Room Temperature Quantum Emission from Cubic Silicon Carbide Nanoparticles

Stefania Castelletto,[†,*] Brett C. Johnson,[‡] Cameron Zachreson,[§] David Beke,[⊥] István Balogh,[⊥] Takeshi Ohshima,[∥] Igor Aharonovich,[§] and Adam Gali[⊥,#]

[†]School of Aerospace, Mechanical and Manufacturing Engineering, RMIT University, Melbourne, Victoria 3000, Australia, [‡]Centre for Quantum Computation and Communication Technology, School of Physics, University of Melbourne, Melbourne, Victoria 3010, Australia, [§]School of Physics and Advanced Materials, University of Technology Sydney, Ultimo, New South Wales 2007, Australia, [⊥]Institute for Solid State Physics and Optics, Wigner Research Center for Physics, Hungarian Academy of Sciences, P.O. Box 49, H-1525 Budapest, Hungary, [∥]SemiConductor Analysis and Radiation Effects Group, Japan Atomic Energy Agency, 1233 Watanuki, Takasaki, Gunma 370-1292, Japan, and [#]Department of Atomic Physics, Budapest, University of Technology and Economics, Budafoki út 8, H-1111, Budapest, Hungary,

ABSTRACT The photoluminescence (PL) arising from silicon carbide nanoparticles has so far been associated with the quantum confinement effect or to radiative transitions between electronically active surface states. In this work we show that cubic phase silicon carbide nanoparticles with diameters in the range 45−500 nm can host other point defects responsible for photoinduced intrabandgap PL. We demonstrate that these nanoparticles exhibit single photon emission at room temperature with record saturation count rates of 7×10^6 counts/s. The realization of nonclassical emission from SiC nanoparticles extends their potential use from fluorescence biomarker beads to optically active quantum elements for next generation quantum sensing and nanophotonics. The single photon emission is related to single isolated SiC defects that give rise to states within the bandgap.

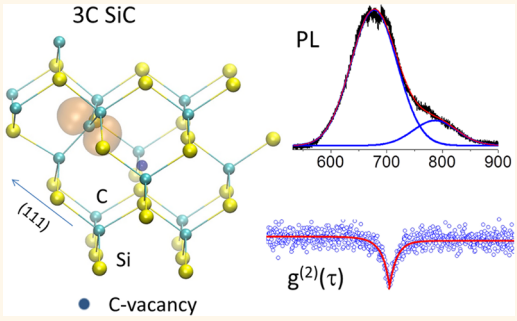

KEYWORDS: silicon carbide · nanoparticles · single photon emission · quantum characterization · intrinsic defects in silicon carbide

Silicon carbide (SiC) is a group IV wide band gap semiconductor with outstanding physical properties for electronic and mechanical applications.[1] SiC exists in many polytypes, with 3C being the most popular for electronics due to the ability to grow it epitaxially on a silicon substrate.[1] Here, 3C refers to its cubic crystal structure that may be built from a hexagonal lattice in the basal plane, and three Si−C bilayers of this hexagonal lattice can be placed in face-centered cubic arrangement along the (0001) direction in the hexagonal lattice nomenclature, which corresponds to the (111) direction in a cubic lattice (see Figure 1a,b). Si−C bilayers can be grown with hexagonal close-packed inclusions too, in an ordered fashion, resulting in other polytypes. The most studied polytypes are 4H and 6H hexagonal polytypes with large bandgaps of 3.2 and 2.9 eV, respectively, compared with the 2.4 eV bandgap of 3C polytype. The point defects and luminescence centers have been well characterized in the hexagonal polytypes that are presently employed in high-power electronics. In contrast, much less is known about the 3C polytype in this respect. Because of the indirect band gap, bulk SiC polytypes were once regarded as having "weak" emission properties, even though the first light emitting diodes (LED) were based on this material. Quantum confinement effects and the formation of a direct bandgap in SiC quantum dot nanoparticles have led to enhanced photoluminescence[2,3] where visible emission came from the 3C polytype. This has stimulated intensive studies on their synthesis and the identification of promising applications in electronics, LEDs and biomedical applications such as drug delivery and bioimaging.[2−5] However, the peak emission wavelengths of the 3C-SiC QDs are in the UV-green spectral region (typically between 380 to 550 nm),[6−9] which is not ideal for biomedical applications due to the overlap with the cell autofluorescence.

* Address correspondence to stefania.castelletto@rmit.edu.au.

Received for review April 1, 2014 and accepted July 18, 2014.

Published online July 18, 2014
10.1021/nn502719y

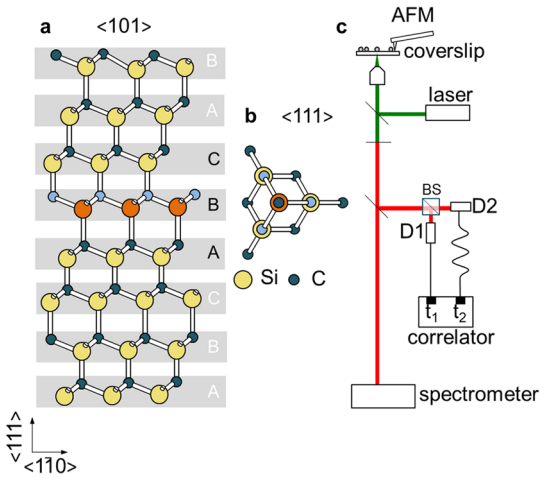

Figure 1. Stacking sequence of the 3C-SiC atoms with (a) (101) and (b) (111) projections constructed by starting and ending with the carbon atoms in bilayer A and bilayer C, respectively. (c) A confocal microscope is aligned with an atomic force microscope for the simultaneous imaging of 3C-SiC nanoparticles dried on a cover glass. Emitted light is directed either to a spectrometer or a Hanbury-Brown and Twiss interferometer.

Recently, very bright photoluminescence (PL) in ultrapure bulk 4H-SiC has been discovered and identified with an intrinsic defect known as the carbon-antisite vacancy pair.[10] This isolated single point defect yields the signature of single photon emission. This result together with progress in the nanofabrication of these materials[11,12] are stimulating further studies on intrinsic defects in their nanostructured counterparts and in different polytypes. Moreover, several SiC defects have shown the possibility of coherent optical spin control, such as the Si-vacancy in hexagonal SiC polytypes[13] and divacancy.[14,15] These defects and other extrinsic defects based on the incorporation of vanadium, molybdenum, and tungsten can be theoretically stable in few nanometers size 3C-SiC quantum dots.[6]

In this paper, we study single photon emitters in 3C-SiC. This is the first demonstration of such emitters in this polytype. SiC polytypism poses both challenges and major advantages in terms of defect deployment and the study of quantum systems. For the application of SiC in quantum technologies, it is of paramount importance to determine the physical properties of potentially interesting defects in all technologically advanced polytypes.[14] In this paper we demonstrate that 3C-SiC nanoparticles can host single quantum systems based on deep defects, opening new avenues for 3C-SiC in quantum technologies in addition to quantum nanophotonics. We attribute the defect responsible for the single photon emission to a carbon antisite vacancy pair, which exhibits a completely different PL recombination mechanism compared to its 4H counterpart.[10] This identification sheds light on an as yet poorly understood deep photoluminescent defect in the 3C polytype. Finally, because of the well-established methods to produce SiC QDs and the predicted stability of many deep defects within SiC materials of this size,[6] our work further suggests extensions to applications in bioimaging.

RESULTS AND DISCUSSION

Atomic Force and Confocal Microscopy Nanoparticles Characterization. Here we report the first observation of room temperature single photon emission from SiC nanoparticles (NPs). Two sources of SiC nanoparticles are examined: commercial 3C-SiC nanopowders suspended in ethanol and large (50−500 nm) SiC nanocrystals (see Supporting Information) that we have synthesized and suspended in Milli-Q both subsequently dried on a glass coverslip. Room temperature confocal microscopy combined with atomic force microscope (AFM), low temperature Raman spectroscopy and cathodo-luminescence were used to characterize the nanoparticles. A schematic of the single photon characterization setup is shown in Figure 1c. CW lasers pump at 532 and 660 nm were used to excite the samples. Further details are provided in the Methods.

The red fluorescence emission from the NPs was sent to a spectrometer or to a Hanbury-Brown and Twiss interferometer to measure the second order correlation function $g^{(2)}(\tau)$. In Figure 2e, a characteristic $g^{(2)}(\tau)$ of the commercial untreated NPs is shown, with $g^{(2)}(0) < 0.5$ indicating single photon emission.

We now discuss the characteristics of the single photon emission in 3C-SiC in the two different types of nanoparticles as well as the impact of the nanoparticle synthesis method indicating that the source of single emitter is a common defect. Figure 2(a,b) shows a confocal map and an AFM map of the same area of as-received commercial 3C-SiC NPs suspended in ethanol and dried onto a coverslip. The confocal map shows strong fluorescence. We observed isolated stable PL from NPs with diameters of around 150 nm (as shown in Figure 2c) even from as-received material. The as-received NPs were also electron irradiated (see Methods) to create vacancies and their PL properties were compared with the as-received material.

The peak of the broad-band room temperature emission was fitted with the convolution of three Gaussian curves indicating the presence of a peak centered at 650 nm (see Figure 2a), here associated with a previously observed visible line in bulk 3C-SiC (see Supporting Information). Because of the unresolved spectral features, filtering is challenging, as evident in the background PL of the $g^{(2)}(\tau)$ curves. The peak position of the total PL line-shape arising from the nonirradiated NPs varies from 673 to 721 nm (see Supporting Information). Irradiation induces a broadening and a red shift of this peak, which is likely associated with the introduction of an amorphous fraction of the nanocrystallites, as shown by Raman

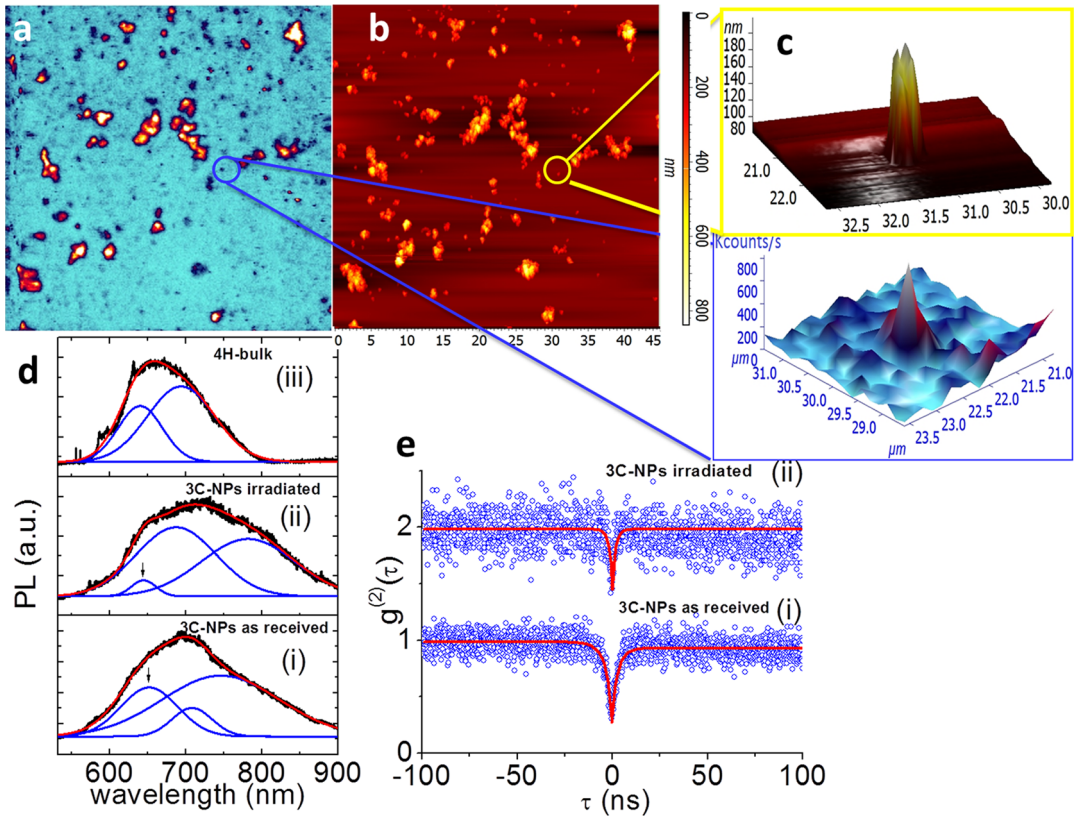

Figure 2. (a) Confocal and (b) AFM 45 × 45 μm^2 images of the same sample area corresponding to as-received SiC NPs dispersed in ethanol before annealing. The confocal image indicates aggregation up to 800 nm. (c) 3D profile of the AFM image and confocal PL image showing the NP around 150 nm in height associated with single photon emission in (e) (i). (d) Typical single photon emitter PL from irradiated (ii) and as-received (i) NPs. Multipeaks Gaussian convolution fits indicate the presence of three main emission peaks. The arrow indicates the presence of a peak at 645−650 nm, here correlated to a similar spectral emission in the bulk material. A dominant peak at 750 nm is present. (iii) PL from a carbon antisite vacancy pairs[10] observed in 4H-SiC is shown at the same 532 nm excitation wavelength, fitted only with two Gaussian profiles. (e) Second order photon autocorrelation of the NP from the confocal-AFM scan (a,b,c) and PL (i) and of two emitters observed in the irradiated sample (ii) (confocal and AFM not shown). The upper plot was shifted up for clarity. Note that the data are not corrected for the background.

spectroscopy (see Supporting Information), which spectrally overlaps with the observed defect and responsible for photobleaching.

A comparison with the single photon emission reported from bulk 4H-SiC PL,[10] is also shown in Figure 2d, indicating that the observed emission from 3C-SiC NPs is similar, but slightly red-shifted compared to the defect observed in bulk 4H-SiC. Presently, there is no reference in the literature to the carbon-antisite vacancy pair in irradiated bulk 3C-SiC.[16,17]

Figure 2e shows the photon correlation function $g^{(2)}(\tau)$ indicating single photon emission ($g^{(2)}(0) < 0.5$) in as-received (i) and irradiated samples (ii). The irradiated NPs were not annealed. The single photon emission was very rarely observed in irradiated samples where instead $g^{(2)}(0) \geq 0.5$ (ii), indicating multiple defects and higher background.

The as-received nanoparticles under confocal inspection show photobleaching due to amorphous material and the single emitter life was typically short (a few minutes). To improve the photostability, we performed air oxidation in a furnace at atmospheric pressure on deposited NPs on a cover-glass for up to 3 h at 550 °C to remove amorphous material from the surface. A remarkable increase in the photostability of the single NP was observed and allowed us to achieve a uniform distribution of isolated NPs on a cover-glass, as shown in Figure 3(a,b,c), with less evidence of agglomeration. The irradiated commercial NPs were also studied after oxidation showing an enhanced PL emission. Figure 3 compares confocal maps of (a) commercial nonirradiated NPs, (b) noncommercial[18] 50−500 nm acid cleaned NPs, and (c) commercial irradiated NPs. All the NPs have undergone the same air oxidation process. In the Supporting Information we show the time traces of exemplary emitters in as-received material and oxidized material. The oxidation process extends the life of the emitters, while emitters in the as-received material are very short-lived and in most cases photobleach.

In Figure 3d the effect of oxidation for 3 h at 550 °C is shown for the PL of single emitters in (i) commercial NPs, (ii) a single emitter in 200 nm 3C noncommercial acid cleaned NPs, and (iii) commercial irradiated NPs.

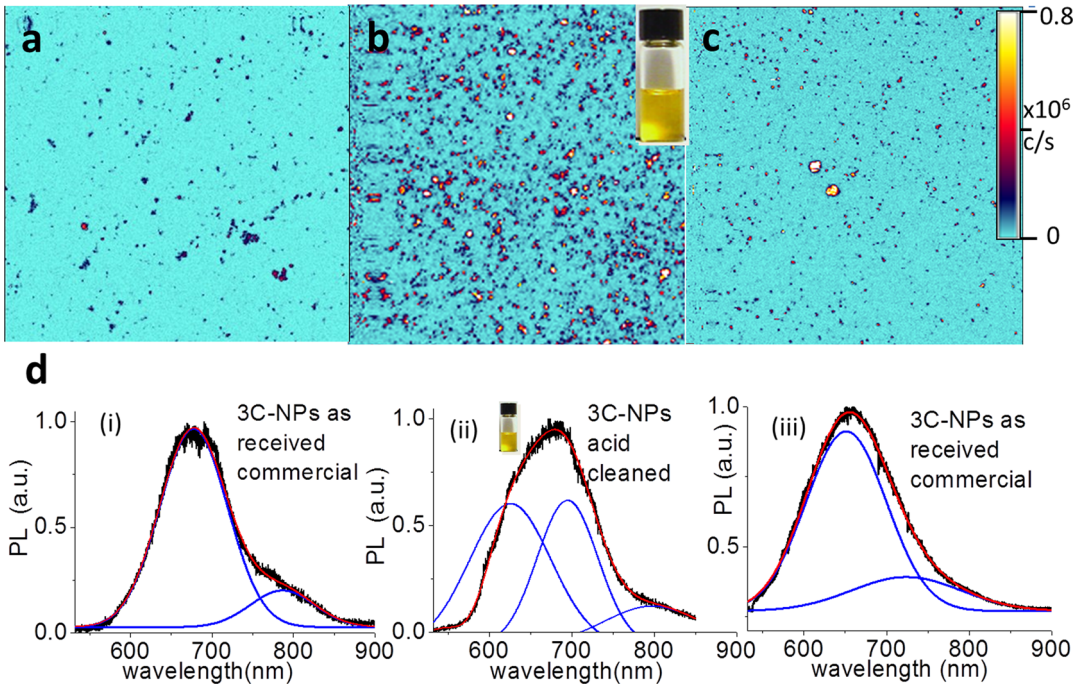

Figure 3. 100 × 100 μm^2 confocal scan of the same concentration 1 mg/5 mL of SiC NP after a 3 h oxidation at 550 °C for (a) as-received commercial NPs, (b) acid cleaned,[18] (c) commercial irradiated NPs at 1 × 10^{17} e/cm^2. (d) PL of single emitters after the 3 h oxidation at 550 °C for (i) as-received commercial NPs, (ii) acid cleaned, (iii) commercial irradiated NPs at 1 × 10^{17} e/cm^2.

The oxidation causes the general PL line-shape to shift to lower wavelengths resulting in peak positions to be centered around 650 nm independent of the NP type, (see Supporting Information for further details). These line shapes also become narrower and typically only require two Gaussian curves to fit the spectra, a dominant peak at 650 nm and a second one 750−800 nm. Blue-shifted PL were also observed after the oxidation of SiC quantum dots.[19]

Single Photon Dynamics of the Defect. We fully characterized the single emitters in 3C NPs in terms of the emission count rate. From the photon autocorrelation function we determined the existence of a shelving state. We excited several single emitters at different optical powers to determine the saturation curve given by $\Phi = \Phi_\infty P_{opt}/(P_{sat} + P_{opt})$.

After oxidation, single NPs exhibited count rates of up to 2.5 × 10^6 counts/s at 0.5 mW incident optical power. For this particular center the saturation count rate and optical saturation power are Φ_∞ =7 × 10^6 counts/s and P_{sat} =0.9 mW, respectively. This is obtained from fitting the data in Figure 4a. This is 1 order of magnitude higher than in bulk 4H-SiC,[10] as might be expected due to the improved photon collection of emission from NPs, where the high refractive index material interface induces internal reflection.[20] We studied the excitation power dependence of the photon correlation function of single defects to deduce the decay rates from the excited state to the metastable state and back to the ground state. As an example Figure 4(b) shows the antibunching behavior of the center with PL shown in Figure 3d(i), for two excitation powers at 532 nm. Because of the presence of a photon-bunching effect (higher correlation at longer delay times), each curve was fit with a three-level system model, where the second-order correlation function is expressed as the sum of two exponentials,

$$g^{(2)}(\tau) = c - ae^{-\tau/\tau_1} + be^{-\tau/\tau_2} \quad (1)$$

with τ_1 and τ_2 being free parameters and related to the transition rates, r_{ij}, from level (*i*) to level (*j*) by the following equations: $1/\tau_1 = r_{12} + r_{21}$, $1/\tau_2 = r_{31} + r_{23}r_{12}\tau_1$.[21] Photon-bunching at longer delay times in single molecules,[22] color centers in diamond[23] and bulk silicon carbide[10] has been associated with the presence of a long-lived metastable state. By fitting the $g^{(2)}(\tau)$, the time constant $\tau_{1,2}$ are obtained at different excitation powers. We used a linear fitting of $\tau_{1,2}^{-1}$ plotted *versus* the optical power. We extrapolate the spontaneous emission lifetime of the excited state decay to the ground state at zero incident power, $\tau_1^0 = 2.04 \pm 0.08$ ns. This term accounts for both radiative and nonradiative decay of higher energy states to the excited state due to the nonresonant excitation. This particular single emission was observed in an oxidized sample. The same linear fitting of τ_2^{-1} provides the lifetime of the nonradiative emission of the excited state to the ground state *via* the metastable state shelving, this lifetime is estimated to be 775 ± 162 ns (Figure 4c), albeit with a 20% associated uncertainty. The residual high uncertainty in the metastable dynamics can be due to some instrumental artifact in the presence of the high count

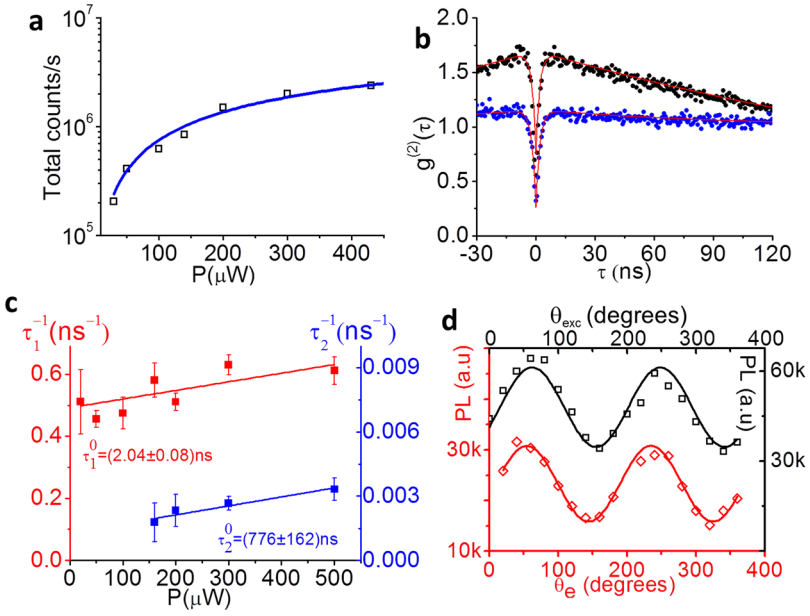

Figure 4. (a) Saturation curve with 2.5 × 10^6 counts/s at 500 μW, and a saturation count rate of 7 × 10^6 counts/s at a saturation excitation pump of 800 μW. (b) Second order background uncorrected photon autocorrelation at 50 and 500 μW excitation power indicating the presence of a third-level metastable state. (c) Estimation of the spontaneous emission lifetime of the excited state and of the nonradiative emission *via* the metastable state obtained from a linear fitting of $\tau_{1,2}^{-1}$ parameters and by its zero optical power intersection. (d) Single defect PL emission polarization (bottom curve in red) at fixed excitation laser polarization and PL obtained by varying the excitation beam polarization (upper curve in black).

rate or to some noise in the data due to fast blinking over the same time scale.

The estimated typical spontaneous emission lifetime of the as-received NPs single photon emission without undergoing oxidation is (3.3 ± 0.2) ns, indicating that oxidation could introduce nonradiative channels on the excited state decay. The irradiated NPs without annealing show a shorter lifetime of ∼0.8 ns, possibly indicating the presence of surface quenching effects introduced by irradiation. An increased lifetime of up to (5.3 ± 0.2) ns was observed in oxidized and acid cleaned samples, but more statistics correlating size effects of the nanoparticles with the lifetime distribution are needed to fully determine the origin of this variation and is beyond the scope of the present work.[24] An example of photon-correlation from different types of nanoparticles at 100 μW excitation power is shown in the Supporting Information. In Table 1 a summary of the measured lifetimes is provided.

We measured the PL polarization by changing the excitation laser polarization and the PL emission polarization at a fixed excitation laser polarization (Figure 4d). The PL of single emitters is partially polarized in excitation and emission indicating the presence of more than one dipole. The degree of the polarizations are I_{min}/I_{max} = 0.27, 0.56 for the emission and excitation, respectively. For a unique determination of the dipole orientation in the laboratory reference frame, radial polarization should be used; however, from the linear polarization we can estimate the angles between the combined dipoles orthogonal axis and the optic axis of the experimental setup to be $\theta = \cos^{-1}((I_{min})/(I_{max}))^{1/2} = (58 \pm 1)°$, $(41 \pm 1.5)°$ for emission and excitation, respectively. For the azimuthal angle of the dipoles orthogonal axis orientation the linear polarization is ambiguous to 180° rotation; however, from the minimum of the PL we deduce that $\phi = 144 \pm 1°$, $155 \pm 1°$ for emission and excitation.

TABLE 1. Comparison of the Lifetime of the Excited and Metastable State of Single Defects for Different Nanoparticles Treatment at 100 μW Excitation Power[a]

material	τ_1 (ns)	τ_2 (ns)
oxidized	2.1 ± 0.1	283 ± 85
as-received	3.3 ± 0.2	309 ± 62
oxidized and acid cleaned	5.3 ± 0.2	305 ± 60

[a] As expected, only the excited state should be affected by the NPs treatment process.

Investigation of the Defect Origin *via* Cathode-Luminescence and Ensemble Spectroscopy. We now discuss the origin of the observed single photon emission in the NPs in relation to previous PL studies on deep defects in 3C-SiC.[25,26] The complete identification of this defect is complicated by the presence of surface states on the NPs. Moreover, no evidence of this sub-bandgap PL emission in NPs is reported in the literature. Since our 3C NPs are large, quantum confinement effect due to size do not occur and the PL should be comparable to the bulk counterpart. Studies of background defects in 3C-SiC have been conducted on epitaxial layers grown on silicon substrates.[27,28] PL in 3C-SiC films epitaxially

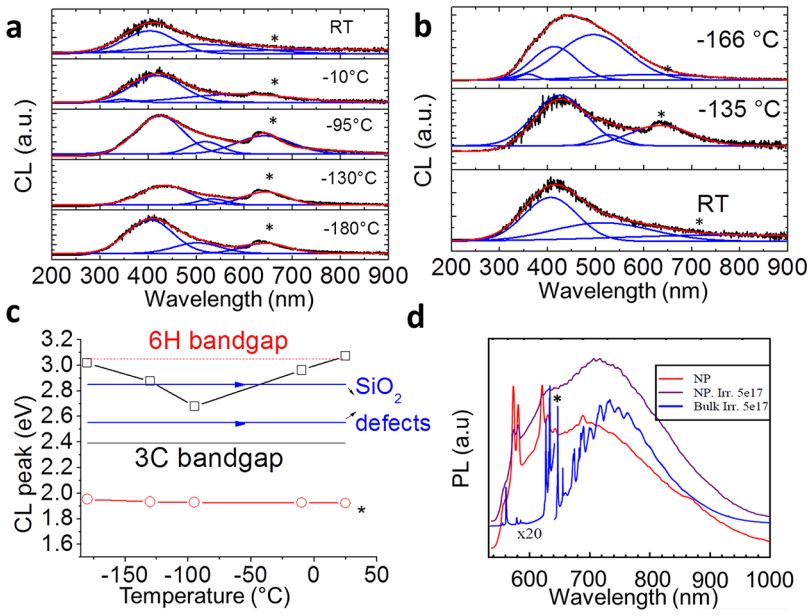

Figure 5. CL spectra at different temperatures of the (a) irradiated and (b) nonirradiated NPs at an acceleration of 2 kV and a current of 74 nA. The spectra show two or three dominant peaks, the peak at 645 nm indicated with (*) corresponds to the here studied single photon defect emission. (c) Dominant peak and the defect of interest peak *versus* the temperature. The band-to band energy of 3C and 6H polytype are shown as well as the energy region where SiO_2-related CL peaks are expected. (d) Ensemble PL at 80 K of 3C-SiC as-received and irradiated NPs compared to irradiated 3C bulk SiC. * indicates a ZPL attributed to 648 nm E-line.[25]

grown on Si substrates was previously reported.[25,28] PL lines induced by irradiation were observed mainly in the photon energy range below 2.0 eV. A common PL line at 628 nm (1.973 eV) has been found in 3C-SiC and is associated with the D_I center, common in all polytypes, found in irradiated and in as-grown material. This defect has a high thermal stability (to above 1400 K), and its luminescence has been associated with the transition from the conduction band edge to a defect level lying ~0.3 eV above the valence band edge introduced by the silicon antisite.[29,30] A dominant PL line (ZPL) at 648 nm (1.913 eV), the so-called E center, has been observed in 3C-SiC irradiated with electrons.[25] This E-center has been attributed to silicon vacancies. However, PL associated with silicon vacancies in 4H and 6H-SiC polytypes occurs in the near-IR throwing doubt on this assignment.[31] In fact, a radiation-induced PL band with a zero-phonon line at 1106 nm (1.121 eV)[32] has been observed in bulk 3C-SiC and also related to a silicon vacancy. We consider the assignment of the E-line with a particular defect in more detail in the next section.

The single photon emission observed here can be associated with the E-line found in the bulk material. However, since we observed the PL in NPs, we should exclude the possibility that this emission is associated with the recombination at defects residing at the interface between SiC and the native surface oxide or even associated with the oxide itself, as type I quantum well PL was observed in 3C core–shell nanowires.[33] To study this possibility we performed cathodo-luminescence (CL) measurements at room and low temperatures on the irradiated and unirradiated samples, as described in the Methods. In Figure 5(a,b) we show the CL spectra of irradiated and nonirradiated NPs at various temperatures fit by multiple Gaussian profiles. Two prominent peaks are present. The first corresponds to above bandgap energy 415–434 nm (2.86–2.99 eV) where the bandgap of bulk 3C-SiC is 2.39 eV corresponding to a wavelength of 519 nm. This peak could be associated with the presence of oxide defects or nanometric inclusions of other polytypes such as 6H, the latter very unlikely as X-ray diffraction data did not show any sign of polytype inclusions either in the as-received or in the synthesized samples. The second peak at 645 nm is associated with a SiC defect, and is likely responsible for the single photon emission. This peak is more evident in the irradiated sample. For example, the CL intensity of the 645 nm emission at −135 °C is enhanced by more than 50% with respect to the same peak in the unirradiated sample. Moreover, the CL intensity at 645 nm tends to increase at lower temperatures. The observation of the dominant peak at 645 nm in irradiated NPs CL, suggests its correlation with the E-line, also observed in irradiated bulk 3C-SiC[27] using CL. Our CL also indicates the presence of silicon oxide defects in our irradiated and nonirradiated NPs, as oxide-related defect PL has been found previously using CL at 2.55 and 2.85 eV.[33] Figure 5c shows there is some dependence of the 645 nm emission with temperature (at room temperature the peak is red-shifted), while we observed an intensity reduction of the CL for the red emission line at lower

temperatures. We found similar properties for the carbon antisite-vacancy complex in bulk 4H-SiC.[10] Therefore, the oxide is not believed to be responsible for this defect since the oxide CL peaks are at shorter wavelengths. In addition, the oxidation process is believed to improve the photostability of the defects by possibly trapping charge carriers similarly to core−shell quantum dots.

To fully correlate the observed single photon emission in NPs to the E-line defect and to determine the effectiveness of the irradiation on the NPs, we performed ensemble spectroscopy measurement at room and at 80 K on electron damaged bulk 3C material and NPs. Both D_I and E lines were produced in the bulk 3C-SiC sample (see Supporting Information). Figure 5d shows the PL in untreated and irradiated NPs at 80 K, compared to the irradiated PL in our bulk material. The PL observed in the untreated NPs at 80K shows the presence of sharp ZPLs at 648 nm (E-line). The irradiated NPs present some spectral structure indicating the possible presence of ZPLs at 80K.

From this study we conclude that the single defect observed is an intrabandgap defect in 3C-SiC correlated to the E-line (centered at 644−645 nm) as clearly observed from PL and CL of as-received and enhanced by electron irradiation. In light of the disagreements in the literature as to the origin of the E-line in 3C-SiC, we use advanced modeling of various candidate defects in the next section to identify the responsible defect.

Defect Density Functional Theory Modeling. To identify the E-line in 3C-SiC, we performed spin-polarized density functional theory (DFT) plane wave supercell calculations to confirm the origin of the E-line PL. The details about the methodology are described in the Methods. We considered two candidate defects: the isolated Si-vacancy (due to the previous assignment) and its counterpart,[17] the carbon antisite-vacancy pair in bulk 3C-SiC (this can be conceptually formed by moving an adjacent C atom into the Si vacancy). The Si-vacancy has T_d symmetry in 3C-SiC where the defect introduces a fully occupied a_1 level and a partially occupied t_2 triple degenerate level in the bandgap. The a_1 level is only visible in the bandgap in the spin minority channel. In the neutral charge state the t_2 level is occupied by two electrons while it is occupied by three electrons in its negative charge state. The spin state of the defect was previously discussed in the literature.[34,35] Here we applied $S = 1$ spin state for the neutral charge state, which may cause about 0.1 eV inaccuracy in its total energy. A doubly negative charge state may be possible if the t_2 level is occupied by four electrons ($S = 1$). Accordingly, the calculated acceptor (0|−) and (−|2−) charge transition levels are at E_V +1.5 eV and E_V +2.2 eV, respectively, where E_V is the valence band maximum. We also calculated the excitation energy of the single negatively charged Si-vacancy where the excited state was formed by promoting an electron either from the a_1 level or the valence band edge to the t_2 level in the spin minority channel. The latter process has lower energy at 2.2 eV which basically agrees with the calculated (−|2−) charge transition level. This is about 0.3 eV larger than the measured ZPL energy of the E-line at ∼1.913 eV (or 648 nm) that is outside the expected uncertainty of the applied methodology (see Methods). The carbon antisite-vacancy pair has C_{3v} symmetry in 3C-SiC lattice (see Figure 6b). Because of the relatively small bandgap of 3C-SiC, the double positive charge state and the single positive charge state of the defect play a role. The neutral charge state is only marginally stable in highly *n*-type doped 3C-SiC. In the (2+) charge state the a_1 level localized on the dangling bond of the carbon antisite is empty while it is singly occupied in (+) charge state. The calculated (2+|+) charge transition level is at 1.95 eV which is very close to the ZPL energy of the E-line. Thus, the PL signal can be understood as the recombination of the singly occupied a_1 defect level and the hole in the valence band edge (see Figure 6a). Indeed, the carbon antisite-vacancy pair has a (2+) charge state under typical measurement conditions according to our calculations, and the electron from the valence band edge can be excited to the empty a_1 defect level of the defect. We note that this is a distinct process than the one proposed for the case of the single photon sources observed in 4H-SiC[10] which may be understood by the large bandgap difference between the host 3C-SiC (2.4 eV) and 4H-SiC (3.2 eV).

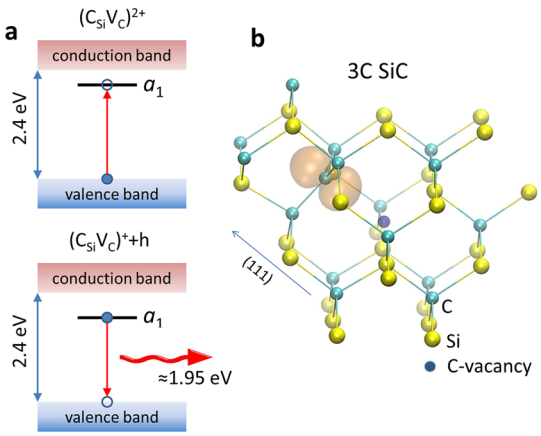

Figure 6. (a) Schematic diagram about the a_1 defect level in the bandgap introduced by the carbon antisite-vacancy pair in its double positive charge state. After exciting an electron from the valence band edge to the defect level, the recombination of the electron occupying this a_1 defect level and the hole left in the valence band edge is responsible for the PL of the single photon emission. (b) Cartoon of the carbon antisite-vacancy pair defect in 3C-SiC. The defect state is localized on the carbon antisite part of the defect, which is close to a sp^2 orbital (orange lobe) pointing along the C_{Si}−V_C axis parallel to the (111) direction of the lattice with exhibiting C_{3v} symmetry. The C_{Si} atom relaxes strongly outward from its lattice site and forms almost a planar configuration with the three nearest neighbor carbon atoms.

CONCLUSIONS

In summary, our study shows for the first time that 3C-SiC nanoparticles can host defects yielding single photon emission. We observed this single photon emission in commercial and noncommercial SiC NDs, without and with electron irradiation. We observed an enhanced PL from irradiated samples and the occurrence of more than one defect in irradiated NPs as per single photon correlation measurements. CL measurements revealed an enhanced intensity of the corresponding defect peak in the irradiated sample. Upon annealing in air at 550 °C we observed an increased photostability in the as-received commercial and acid cleaned in-house synthesized NPs. The sub-bandgap emission in conjunction with the CL data indicate that the single photon PL is a deep defect in SiC correlated to previously observed emission in bulk 3C-SiC known as the E-line. Its observation in SiC NPs produced with different synthesis types indicates that it is a common defect. From irradiated bulk 3C-SiC material PL measurements, a room temperature broad emission centered at 750 nm is observed with a ZPL at 648 nm becoming apparent at low temperatures. Because of the conflicting assignments of this defect in the literature, we performed modeling of both the silicon vacancy and carbon-antisite vacancy pair. Our *ab initio* simulation indicates that the defect associated with the E-line is the carbon-antisite vacancy pair, which exhibits a completely different recombination mechanism from its 4H counterpart. The observed brightness and easy availability in this material of stable, very bright single defects constitute a relevant advance in the observation of single photon emitters in wide-bandgap semiconductor NPs, with the possibility of incorporation into SiC QDs. In addition, this work signifies the first observation of a single defect in 3C-SiC, which is presently a relevant polytype for the fabrication of photonics crystal cavities and high-Q optical microdisks.[36−38] The integration of the described single defects into these photonic devices and other hybrid systems[39] may also be a promising way to realize a range of future devices with quantum functionalities.

METHODS

SiC faceted spherical nanoparticles with an average particle size of 45−55 nm and purchased from Nanostructured & Amorphous Materials, Inc., were synthesized by plasma CVD and may have up to a 15% amorphous content. Other larger SiC NPs were synthesized from Silicon (Across, 365 mesh) and graphite powder according to the procedure described in ref 18. The latter were suspended in water and treated using a mixture of hydrofluoric acid (HF) and nitric acid (HNO_3) at elevated temperature. Some of the commercial NPs were also irradiated with 2 MeV electrons to a fluence of 1×10^{17} e/cm^2. The samples were held at temperatures below 80 °C during irradiation in a nitrogen ambient. After irradiation, no anneal was performed. The nanoparticles were mixed with pure ethanol in a concentration of 1 mg/5 mL, sonicated for 20 min and drop-dry on plasma etched cover-glass. The larger nanoparticles dispersed in Milli-Q were spin coated on a clean cover glass to achieve a homogeneous distribution of well dispersed NPs. Similar irradiation procedures were used to create the defects in bulk 3C-SiC epilayers.

The sample image was simultaneously measured with a confocal scanning fluorescence microscope (100× oil immersion objective lens, NA 1.4), excited with a 532 nm CW diode pumped solid-state laser, and a commercial atomic force microscope (AFM). A spectrometer with a cooled CCD was used to record the photoluminescence (PL) and a Hanbury-Brown and Twiss (HBT) interferometer with single-photon-sensitive avalanche photodiodes was used to measure the photon statistics. Photon counting and correlation were carried out using a time-correlated single photon-counting (TCSPC) module. Another confocal system was used with multiple excitation wavelengths. The PL from NPs was collected using a sharp edge high optical density and low fluorescence Semrock long pass filter, without the use of any additional bandpass filter, allowing the maximum photon transmission.

A Renishaw InVia Micro-Raman Spectrometer equipped with a Linkam stage for temperature control was used for the ensemble PL measurements. A 532 nm laser was directed through a 20× long working distance objective with a 0.4 NA onto the sample. The laser power at the sample was approximately 0.5 mW.

Cathodo-luminescence measurements were performed at room and low temperature (80 K) using an FEI Quanta environmental SEM equipped with a liquid nitrogen cooling stage. A parabolic mirror (Gatan) directed light through an ex-situ focusing lens onto a 600 nm optical fiber coupled to a spectrophotometer (OceanOptics QE65000) with a bandpass of 6.5 nm.

Density functional theory plane wave supercell calculations were applied to identify the E-line in 3C-SiC. We modeled the defect in a 512-atom simple cubic supercell. The Γ-point was sufficiently convergent to map the Brillouin-zone in this large supercell. We applied the nonlocal screened hybrid density functional of Heyd-Scuseria-Ernzerhof with a mixing parameter of Hartree−Fock exchange of 0.25 and the screening parameter of 0.2 1/Å.[40] The geometry of the defects was optimized to find the minimum energy of the system until the quantum mechanical forces on the atoms were less than 0.01 eV/Å. We applied the 2/3 of the monopole term of the Makov-Payne correction for the total energy of charged supercells.[41] This methodology provides accurate charge transition levels for deep defects within 0.1 eV in Group-IV semiconductors.[42] The excitation energy was calculated by the Δ*S*CF method.[43] We used a plane wave basis set to describe the valence electrons with a projector augmented wave method.[44] We use a kinetic energy cutoff of 420 eV in the expansion of plane waves as implemented in VASP code.[45]

Conflict of Interest: The authors declare no competing financial interest.

Acknowledgment. S.C. acknowledges initial financial support from the Australian Research Council, Centre of Excellence Engineered Quantum Systems (CE110001013). B.C.J. acknowledges the Australian Research Council Centre for Quantum Computation and Communication Technology (CE110001027). I.A. is the recipient of an Australian research council discovery early career research award (project number DE130100592). A.G. acknowledges the dynamic light scattering measurements by Eszter Gergely-Fülöp from the Research Centre for Natural Sciences, the support from the Lendület programme of the Hungarian Academy of Sciences, and the Hungarian OTKA Grants No. K101819 and K106114. D.B. acknowledges the support from the European Union and the State of Hungary, cofinanced by the European Social Fund in the framework of

TÁMOP-4.2.4.A/2-11/1-2012-0001 "National Excellence Program". We acknowledge Kerem Bray, Rodolfo Previdi and Olga Shimoni for assistance with DLS measurements at UTS.

Supporting Information Available: Figures S1−S5. This material is available free of charge *via* the Internet at http://pubs.acs.org.

REFERENCES AND NOTES

1. Nakamura, D.; Gunjishima, I.; Yamaguchi, S.; Ito, T.; Okamoto, A.; Kondo, H.; Onda, S.; Takatori, K. Ultrahigh-Quality Silicon Carbide Single Crystals. *Nature* **2004**, *430*, 1009–1012.
2. Fan, J. Y.; Li, H. X.; Iiang, J.; So, L. K. Y.; Lam, Y. W.; Chu, P. K. 3C-SiC Nanocrystals as Fluorescent Biological Labels. *Small* **2008**, *4*, 1058–1062.
3. Wu, X. L.; Fan, J. Y.; Qiu, T.; Yang, X.; Siu, G. G.; Chu, P. K. Experimental Evidence for the Quantum Confinement Effect in 3C-SiC Nanocrystallites. *Phys. Rev. Lett.* **2005**, *94*, 026102.
4. Mognetti, B.; Barberis, A.; Marino, S.; Di Carlo, F.; Lysenko, V.; Marty, O.; Geloen, A. Preferential Killing of Cancer Cells Using Silicon Carbide Quantum Dots. *J. Nanosci. Nanotechnol.* **2010**, *10*, 7971–7975.
5. Serdiuk, T.; Lysenko, V.; Mognetti, B.; Skryshevsky, V.; Géloën, A. Impact of Cell Division on Intracellular Uptake and Nuclear Targeting with Fluorescent SiC-based Nanoparticles. *J. Biophotonics* **2013**, *6*, 291–297.
6. Somogyi, B.; Zolyomi, V.; Gali, A. Near-infrared Luminescent Cubic Silicon Carbide Nanocrystals for *in Vivo* Biomarker Applications: an *Ab Initio* Study. *Nanoscale* **2012**, *4*, 7720–7726.
7. Botsoa, J.; Lysenko, V.; Geloen, A.; Marty, O.; Bluet, J. M.; Guillot, G. Application of 3C-SiC Quantum Dots for Living Cell Imaging. *Appl. Phys. Lett.* **2008**, *92*, 173902.
8. Beke, D.; Szekrenyes, Z.; Balogh, I.; Veres, M.; Fazakas, E.; Varga, L. K.; Kamaras, K.; Czigany, Z.; Gali, A. Characterization of Luminescent Silicon Carbide Nanocrystals Prepared by Reactive Bonding and Subsequent Wet Chemical Etching. *Appl. Phys. Lett.* **2011**, *99*, 213108.
9. Yang, S. K.; Kiraly, B.; Wang, W. Y.; Shang, S. L.; Cao, B. Q.; Zeng, H. B.; Zhao, Y. H.; Li, W. Z.; Liu, Z. K.; Cai, W. P.; *et al.* Fabrication and Characterization of Beaded SiC Quantum Rings with Anomalous Red Spectral Shift. *Adv. Mater.* **2012**, *24*, 5598–5603.
10. Castelletto, S.; Johnson, B. C.; Ivady, V.; Stavrias, N.; Umeda, T.; Gali, A.; Ohshima, T. A Silicon Carbide Room-Temperature Single-Photon Source. *Nat. Mater.* **2014**, *13*, 151–156.
11. Ho, G. W.; Wong, A. S. W.; Kang, D. J.; Welland, M. E. Three-Dimensional Crystalline SiC Nanowire Flowers. *Nanotechnology* **2004**, *15*, 996–999.
12. Magyar, A. P.; Aharonovich, I.; Baram, M.; Hu, E. L. Photoluminescent SiC Tetrapods. *Nano Lett.* **2013**, *13*, 1210–1215.
13. Kraus, H.; Soltamov, V. A.; Riedel, D.; Vath, S.; Fuchs, F.; Sperlich, A.; Baranov, P. G.; Dyakonov, V.; Astakhov, G. V. Room-Temperature Quantum Microwave Emitters Based on Spin Defects in Silicon Carbide. *Nat. Phys.* **2014**, *10*, 157–162.
14. Falk, A. L.; Buckley, B. B.; Calusine, G.; Koehl, W. F.; Dobrovitski, V. V.; Politi, A.; Zorman, C. A.; Feng, P. X. L.; Awschalom, D. D. Polytype Control of Spin Qubits in Silicon Carbide. *Nat. Commun.* **2013**, *4*, 1819.
15. Koehl, W. F.; Buckley, B. B.; Heremans, F. J.; Calusine, G.; Awschalom, D. D. Room Temperature Coherent Control of Defect Spin Qubits in Silicon Carbide. *Nature* **2011**, *479*, 84–87.
16. Lebedev, A. A. Deep Level Centers in Silicon Carbide: A Review. *Semiconductors* **1999**, *33*, 107–130.
17. Umeda, T.; Son, N. T.; Isoya, J.; Janzén, E.; Ohshima, T.; Morishita, N.; Itoh, H.; Gali, A.; Bockstedte, M. Identification of the Carbon Antisite-Vacancy Pair in 4H-SiC. *Phys. Rev. Lett.* **2006**, *96*, 145501.
18. Beke, D.; Szekrenyes, Z.; Balogh, I.; Czigany, Z.; Kamaras, K.; Gali, A. Preparation of Small Silicon Carbide Quantum Dots by Wet Chemical Etching. *J. Mater. Res.* **2013**, *28*, 44–49.
19. Zakharko, Y.; Botsoa, J.; Alekseev, S.; Lysenko, V.; Bluet, J. M.; Marty, O.; Skryshevsky, V. A.; Guillot, G. Influence of the Interfacial Chemical Environment on the Luminescence of 3C-SiC nanoparticles. *J. Appl. Phys.* **2010**, *107*, 013503.
20. Aharonovich, I.; Castelletto, S.; Simpson, D. A.; Stacey, A.; McCallum, J.; Greentree, A. D.; Prawer, S. Two-Level Ultrabright Single Photon Emission from Diamond Nanocrystals. *Nano Lett.* **2009**, *9*, 3191–3195.
21. Kitson, S. C.; Jonsson, P.; Rarity, J. G.; Tapster, P. R. Intensity Fluctuation Spectroscopy of Small Numbers of Dye Molecules in a Microcavity. *Phys. Rev. A: At., Mol., Opt. Phys.* **1998**, *58*, 620–627.
22. Basché, T.; Moerner, W. E.; Orrit, M.; Talon, H. Photon Antibunching in the Fluorescence of a Single Dye Molecule Trapped in a Solid. *Phys. Rev. Lett.* **1992**, *69* (10), 1516–1519.
23. Kurtsiefer, C.; Mayer, S.; Zarda, P.; Weinfurter, H. Stable Solid-State Source of Single Photons. *Phys. Rev. Lett.* **2000**, *85*, 290–293.
24. Inam, F. A.; Grogan, M. D. W.; Rollings, M.; Gaebel, T.; Say, J. M.; Bradac, C.; Birks, T. A.; Wadsworth, W. J.; Castelletto, S.; Rabeau, J. R.; *et al.* Emission and Nonradiative Decay of Nanodiamond NV Centers in a Low Refractive Index Environment. *ACS Nano* **2013**, *7*, 3833–3843.
25. Itoh, H.; Yoshikawa, M.; Nashiyama, I.; Okumura, H.; Misawa, S.; Yoshida, S. Photoluminescence of Radiation Induced Defects in 3C-SiC Epitaxially Grown on Si. *J. Appl. Phys.* **1995**, *77*, 837–842.
26. Konstantinov, A. O.; Henry, A.; Harris, C. I.; Janzen, E. Photoluminescence Studies of Porous Silicon Carbide. *Appl. Phys. Lett.* **1995**, *66*, 2250–2252.
27. Zhou, P.; Spencer, M. G.; Harris, G. L.; Fekade, K. Observation of Deep Levels in Cubic Silicon Carbide. *Appl. Phys. Lett.* **1987**, *50*, 1384–1385.
28. Zekentes, K.; Kayiambaki, M.; Constantinidis, G. Electron Traps in β-SiC Grown by Chemical Vapor Deposition on Silicon (100) Substrates. *Appl. Phys. Lett.* **1995**, *66*, 3015–3017.
29. Gali, A.; Deák, P.; Rauls, E.; Son, N. T.; Ivanov, I. G.; Carlsson, F. H. C.; Janzén, E.; Choyke, W. J. Correlation between the Antisite Pair and the D_I Center in SiC. *Phys. Rev. B: Condens. Matter Mater. Phys.* **2003**, *67*, 155203.
30. Eberlein, T. A. G.; Jones, R.; Öberg, S.; Briddon, P. R. Density Functional Theory Calculation of the D_I Optical Center in SiC. *Phys. Rev. B: Condens. Matter Mater. Phys.* **2006**, *74*, 144106.
31. Soltamov, V. A.; Soltamova, A. A.; Baranov, P. G.; Proskuryakov, I. I. Room Temperature Coherent Spin Alignment of Silicon Vacancies in 4H and 6H-SiC. *Phys. Rev. Lett.* **2012**, *108*, 226402.
32. Son, N. T.; Sörman, E.; Chen, W. M.; Hallin, C.; Kordina, O.; Monemar, B.; Janzén, E.; Lindström, J. L. Optically Detected Magnetic Resonance Studies of Defects in Electron-Irradiated 3C SiC Layers. *Phys. Rev. B: Condens. Matter Mater. Phys.* **1997**, *55*, 2863–2866.
33. Fabbri, F.; Rossi, F.; Attolini, G.; Salviati, G.; Iannotta, S.; Aversa, L.; Verucchi, R.; Nardi, M.; Fukata, N.; Dierre, B.; *et al.* Enhancement of the Core Near-Band-Edge Emission Induced by an Amorphous Shell in Coaxial One-dimensional Nanostructure: the Case of SiC/SiO2 Core/Shell Self-Organized Nanowires. *Nanotechnology* **2010**, *21*, 345702.
34. Deák, P.; Miró, J.; Gali, A.; Udvardi, L.; Overhof, H. The Spin State of the Neutral Silicon Vacancy in 3C−SiC. *Appl. Phys. Lett.* **1999**, *75*, 2103–2105.
35. Zywietz, A.; Furthmüller, J.; Bechstedt, F. Spin State of Vacancies: From Magnetic Jahn-Teller Distortions to Multiplets. *Phys. Rev. B: Condens. Matter Mater. Phys.* **2000**, *62*, 6854–6857.
36. Radulaski, M.; Babinec, T. M.; Buckley, S.; Rundquist, A.; Provine, J.; Alassaad, K.; Ferro, G.; Vuckovic, J. Photonic Crystal Cavities in Cubic (3C) Polytype Silicon Carbide Films. *Opt. Express* **2013**, *21*, 32623–32629.
37. Cardenas, J.; Zhang, M.; Phare, C. T.; Shah, S. Y.; Poitras, C. B.; Guha, B.; Lipson, M. High Q SiC Microresonators. *Opt. Express* **2013**, *21*, 16882–16887.

38. Magyar, A. P.; Bracher, D.; Lee, J. C.; Aharonovich, I.; Hu, E. L. High Quality SiC Microdisk Resonators Fabricated from Monolithic Epilayer Wafers. *Appl. Phys. Lett.* **2014**, *104*, 051109.
39. Schell, A. W.; Kaschke, J.; Fischer, J.; Henze, R.; Wolters, J.; Wegener, M.; Benson, O. Three-Dimensional Quantum Photonic Elements Based on Single Nitrogen Vacancy-Centres in Laser-Written Microstructures. *Sci. Rep.* **2013**, *3*, 1577.
40. Heyd, J.; Scuseria, G. E.; Ernzerhof, M. Hybrid Functionals Based on a Screened Coulomb Potential. *J. Chem. Phys.* **2003**, *118*, 8207–8215.
41. Lany, S.; Zunger, A. Assessment of Correction Methods for the Band-Gap Problem and for Finite-Size Effects in Supercell Defect Calculations: Case Studies for ZnO and GaAs. *Phys. Rev. B: Condens. Matter Mater. Phys.* **2008**, *78*, 235104.
42. Deák, P.; Aradi, B.; Frauenheim, T.; Janzén, E.; Gali, A. Accurate Defect Levels Obtained from the HSE06 Range-Separated Hybrid Functional. *Phys. Rev. B: Condens. Matter Mater. Phys.* **2010**, *81*, 153203.
43. Gali, A.; Janzén, E.; Deák, P.; Kresse, G.; Kaxiras, E. Theory of Spin-Conserving Excitation of the NV Center in Diamond. *Phys. Rev. Lett.* **2009**, *103*, 186404.
44. Blöchl, P. E. Projector Augmented-Wave Method. *Phys. Rev. B: Condens. Matter Mater. Phys.* **1994**, *50*, 17953–17979.
45. Kresse, G.; Hafner, J. *Ab Initio* Molecular-dynamics Simulation of the Liquid-Metal–Amorphous-Semiconductor Transition in Germanium. *Phys. Rev. B: Condens. Matter Mater. Phys.* **1994**, *49*, 14251–14269.